J. Fluid Mech. (2007), *vol.* 575, *pp.* 149–176. © 2007 Cambridge University Press
doi:10.1017/S0022112006004137 Printed in the United Kingdom

Propagation and stability of vorticity–entropy waves in a non-uniform flow

O. V. ATASSI

University of Seville, Seville, Spain 41092 and Pratt & Whitney, East Hartford, CT 06108, USA

(Received 27 July 2005 and in revised form 7 September 2006)

The evolution of disturbances in an annular duct with a non-isentropic radially varying mean flow is studied. Linear and nonlinear analyses are carried out to examine how the mean velocity and density gradients affect the stability and coupling between the disturbances. To isolate the effect of the mean-velocity gradients from that of the mean-density gradients two mean flows are considered, one with a Gaussian density profile and a uniform axial velocity and the other with Gaussian density and Gaussian axial-velocity distributions. For small-amplitude disturbances with the former mean flow profile, the vortical disturbances convect with the mean flow and density fluctuations grow linearly in space as a result of the interaction of the mean-density gradient with the disturbance radial velocity. Eigenmode analysis of the latter profile shows that unstable modes with exponential growth occur owing to the inflection point in the mean-velocity profile. These modes are almost independent of the mean-density profile and are most unstable for low azimuthal wavenumbers. Nonlinear solutions support the linear results and show an algebraic growth of the density for a range of azimuthal wavenumbers and both uniform and non-uniform mean-velocity profiles. The growth of the velocity fluctuations, however, is strongly dependent on the azimuthal wavenumber of the incident disturbance and the mean-velocity profile. The largest growth in the disturbance is observed at radial locations where the largest mean-flow gradients exist. Owing to the growth of the density fluctuations, coupled vorticity–entropy waves are observed downstream of a forced harmonic excitation in a non-isentropic flow. The forcing amplitudes of the incident waves were varied to see how the solutions change with amplitude. As the amplitude is increased, the waves continue to grow and a steepening of the gradients is observed as they propagate downstream until eventually very sharp density and velocity fronts form. These results show that the mean-flow and density profiles play an important role in the evolution of low-azimuthal-wavenumber disturbances which can couple strongly to the duct acoustic modes during combustion instabilities.

1. Introduction

In a combustor or an augmentor, where the flow is heated, the temperature is not uniform but instead varies significantly across the radius of the duct. These radial variations in temperature produce entropy waves which convect downstream and couple with the vorticity disturbances. While the coupling, growth and propagation of these waves are interesting in their own right, some of the energy can be converted into acoustic energy resulting in strong coupling between acoustic, vorticity and entropy waves and combustion instability. As a preliminary step towards studying combustion instability, we study the propagation and coupling of entropy and vorticity waves propagating in a duct with a non-uniform mean flow.

The evolution of small-amplitude disturbances in a uniform mean flow is well understood (Kovàsnznay (1953)). In this case, disturbances of the linearized Euler equations can be split into independent acoustic, vortical and entropic disturbances. This has also formed the basis for formulating inflow–outflow boundary conditions in numerical schemes since independent conditions can be written for each independent disturbance. When the mean flow is non-uniform, however, the acoustic and vortical disturbances are coupled (Kerrebrock 1977; Golubev & Atassi 1998), making the distinction between what is an acoustic disturbance and what is a vortical or entropic disturbance less clear. However, in many aeroacoustic applications the frequencies of interest are high and the coupling between acoustic and vorticity disturbances is weak. As a result, the disturbances can be treated independently (Atassi 2003) to calculate the propagation of waves in constant area ducts. The analysis can be extended, using the method of multiple scales, to slowly varying cross-sections (Cooper & Peake 2001, 2005; Rienstra 1999; Rienstra & Eversman 2003).

Combustion instabilities occur at low frequencies and are characterized by non-isentropic flow due to heat addition. Previous work motivated by combustion instability has focused on problems where the mean flow varies rapidly in the axial direction and the disturbances have long wavelengths relative to the mean-flow variation. In this limit, the mean flow can be treated as uniform upstream and downstream of the zone of rapid variation separated by jump conditions which connect the mean flows in the two regions. The unsteady problem then is to determine the reflection and transmission of disturbances across the discontinuities (Marble & Candel 1977; Stow, Dowling & Hynes 2002). However, when the hub–tip ratio of the duct is not close to unity, the mean flow exhibits significant variation from hub to tip and both the mean-flow variation and the wavelengths of the incident waves scale with the mean radius of the duct. In this limit, the mean-flow gradients are expected to alter significantly the evolution of the incident vortical and entropic waves.

Owing to the large gradients in entropy that often occur in applications, nonlinear effects are also expected to be important. Recent work has examined nonlinear effects in the propagation of entropy waves in a region with axial entropy gradients (Lin & Szeri 2001; Tyagi & Sujith 2003; Soukhomlinov *et al.* 2002). These works show the classical (Whitham 1974) steepening of waves resulting from the amplitude dependence of the wave speed that occurs when the waves have finite amplitude.

In the present paper, we examine the propagation and stability of vorticity–entropy waves. We first investigate small-amplitude disturbances, which are modelled by the linearized Euler equations, to examine the coupling between the vortical and entropic modes. We then solve the nonlinear Euler equations to study the stability and evolution of the vorticity and entropy waves in a non-isentropic flow. The objective of the paper is to examine (i) the coupling between vortical and entropic waves in a non-uniform flow, (ii) the effect of temperature gradients on the stability of the disturbances and (iii) nonlinear effects on the development of vorticity and entropy waves.

In § 2, we present the mathematical formulation of the problem, which is governed by the nonlinear Euler equations. In § 3, we linearize the Euler equations about an axisymmetric radially varying mean flow. We then examine solutions to the linearized problem to gain some insight into the effects of the mean-flow gradients on the evolution of the disturbances. In § 4, we solve the nonlinear equations numerically and compute the evolution of incident vortical and entropic waves. We also examine how the solutions deviate from the linear results given in § 3. In § 5, conclusions are presented.

2. Mathematical formulation

The mean flow is non-uniform in both temperature and velocity, owing to non-uniform heating and wake defects from upstream structures and flow separation. The unsteady flow is characterized by a dominant angular frequency. We assume that the flow quantities are given at an axial cross-section, $x = x_i$, downstream of which viscous effects, heat conduction and heat addition are negligible. In general, the system is governed by the Euler equations in a volume V bounded by a surface ∂V, which are expressed in conservation form as

$$\frac{\partial}{\partial t}\int_V W_i \,\mathrm{d}\Omega + \int_{\partial V} F^C_{ij} n_j \,\mathrm{d}\Gamma = 0, \tag{2.1}$$

where n_j is the unit normal of the surface ∂V the vector, W_i and tensor F^C_{ij} are the conservation variables and convective fluxes for mass, momentum and energy, respectively. These are given explicitly as

$$\left.\begin{aligned} W_i &= [\rho \quad \rho u \quad \rho v \quad \rho w \quad E]^T, \\ F_{ij} &= [\rho u_j \quad p\delta_{1j} + \rho u u_j \quad p\delta_{2j} + \rho v u_j \quad p\delta_{3j} + \rho w u_j \quad (E + p)u_j]^T, \end{aligned}\right\}$$

where ρ is the density, $u_j = [u \;\; v \;\; w]^T$ are the Cartesian coordinates of the velocity field, F_{ij} is the jth column of the 5×3 matrix F^C_{ij}, p is the pressure and $E = \rho(c_v T + \boldsymbol{v}^2/2)$ is the total energy, with temperature T and specific heat at constant volume c_v. The scheme for solving (2.1) is second-order accurate with a MacCormack time-stepping procedure and uses an artificial dissipation procedure in the vicinity of shocks, as described in Jameson, Schmidt & Turkel (1981).

The geometry is an annular duct whose inner and outer radii are $r = r_h$ and $r = r_t$, respectively. Thus at the surfaces of the duct, $r = r_h$ or $r = r_t$, and at any solid bodies which lie in the computational domain the impermeability condition

$$u_j n_j = 0 \tag{2.2}$$

is locally applied.

We assume that the flow can be locally modelled by the linearized Euler equations near the inflow boundary to represent the incident disturbances and we similarly use a linear convection condition at the outflow boundary. The approach of locally linearizing the equations to impose inflow–outflow boundary conditions has been used successfully in the Euler equations to compute the propagation of acoustic, vortical and entropic waves and the scattering of incident vortical waves by a cascade (Atassi, O. V. & Galan 2005) where the mean flow is uniform near the boundaries. In an isentropic but non-uniform mean flow, inflow–outflow conditions have been derived for the linearized Euler equations in the frequency domain using results obtained from an eigenmode analysis (Atassi, H. M. *et al.* 2004). The results show that the pressure field associated with the nearly convected vortical modes is small. On the basis of this observation, they derived an inflow condition for the vortically dominated disturbances.

Although numerical solutions to (2.1) are presented in § 4, to gain insight into the general solutions we first examine linear solutions to the Euler equations perturbed about a non-uniform mean flow. The linear results are presented in § 3 and provide guidance for the numerical cases examined in § 4.

3. Linear analysis

In this section, we examine the propagation of small-amplitude perturbations in a constant-area annular duct with a non-uniform non-isentropic mean flow to assess (i) the effect of mean-temperature gradients on the solutions and (ii) the parameter space for nonlinear calculations.

We assume that the flow is governed by small perturbations to a non-uniform mean flow and therefore expand the flow quantities as follows:

$$\boldsymbol{U}(\boldsymbol{x},t) = \boldsymbol{U}(\boldsymbol{x}) + \boldsymbol{u}(\boldsymbol{x},t), \tag{3.1}$$

$$p(\boldsymbol{x},t) = p_0(\boldsymbol{x}) + p'(\boldsymbol{x},t), \tag{3.2}$$

$$\rho(\boldsymbol{x},t) = \rho_0(\boldsymbol{x}) + \rho'(\boldsymbol{x},t), \tag{3.3}$$

where $\boldsymbol{x}$ stands for the position vector, t for time, and $\boldsymbol{U}$, p_0, ρ_0 are the steady mean velocity, pressure and density, respectively. The corresponding unsteady perturbation quantities $\boldsymbol{u}$, p', ρ' are such that $|\boldsymbol{u}(\boldsymbol{x},t)| \ll |\boldsymbol{U}(\boldsymbol{x})|$, $|p'(\boldsymbol{x},t)| \ll p_0(\boldsymbol{x})$ and $|\rho'(\boldsymbol{x},t)| \ll \rho_0(\boldsymbol{x})$.

3.1. *Axisymmetric mean flow*

Owing to temperature variations in the flow, the mean density is non-uniform and solely depends on the radial distance r:

$$\rho_0(\boldsymbol{x}) = \rho_0(r). \tag{3.4}$$

The mean flow $\boldsymbol{U}(\boldsymbol{x})$ is assumed to be axisymmetric and of the form

$$\boldsymbol{U}(\boldsymbol{x}) = U_x(r)\boldsymbol{e}_x, \tag{3.5}$$

where U_x is the mean-velocity component in the axial direction and $\boldsymbol{e}_x$ represents the unit vector in the axial direction. Note that a consequence of (3.5) is that the mean flow is divergence free. The mean vorticity is given by

$$\boldsymbol{\zeta} = \nabla \times \boldsymbol{U} = -\frac{\mathrm{d}U_x}{\mathrm{d}r}\boldsymbol{e}_\theta \tag{3.6}$$

where $\boldsymbol{e}_\theta$ represents the unit vector in the azimuthal direction. While, in general, any pressure variations are due to the presence of swirl (circulation) and are governed by

$$\frac{\mathrm{d}p_0}{\mathrm{d}r} = \rho_0\frac{U_\theta^2}{r}, \tag{3.7}$$

for the case of zero mean swirl, which we consider in this paper, the mean pressure is constant throughout the domain, $p_0(\boldsymbol{x}) = p_0$. The total mean enthalpy H_0 can be expressed in terms of the density and velocity using Crocco's relation,

$$\frac{\mathrm{d}H_0}{\mathrm{d}r} = -\left(\frac{1}{(\gamma-1)\rho_0^2}\frac{\mathrm{d}\rho_0}{\mathrm{d}r} + U_x\zeta_\theta\right), \tag{3.8}$$

where γ is the ratio of specific heats. Note that (3.8) suggests that non-uniform density gradients can generate mean vorticity except when the changes in density are exactly balanced by the changes in total enthalpy.

We non-dimensionalize all lengths with respect to the mean radius r_m, all velocities with respect to the speed of sound c_{0m} and the density with respect to ρ_{0m}, where the subscript m refers to conditions at $r = r_m$.

3.2. *Perturbation equations*

The small-amplitude fluctuations are governed by the linearized Euler equations,

$$\frac{\mathrm{D}_0}{\mathrm{D}t}\rho' + \rho_0 \nabla \cdot \boldsymbol{u} + \frac{\mathrm{d}\rho_0}{\mathrm{d}r}u_r = 0, \tag{3.9}$$

$$\rho_0\left(\frac{\mathrm{D}_0}{\mathrm{D}t}u_x + u_r\frac{\mathrm{d}M_x(r)}{\mathrm{d}r}\right) = -\frac{\partial p'}{\partial x} \tag{3.10}$$

$$\rho_0\left(\frac{\mathrm{D}_0}{\mathrm{D}t}u_r\right) = -\frac{\partial p'}{\partial r} \tag{3.11}$$

$$\rho_0\left(\frac{\mathrm{D}_0}{\mathrm{D}t}u_\theta\right) = -\frac{\partial p'}{r\partial \theta} \tag{3.12}$$

$$\frac{\mathrm{D}_0}{\mathrm{D}t}p' + \nabla \cdot \boldsymbol{u} = 0, \tag{3.13}$$

where $\rho', u_x, u_r, u_\theta, p'$ are the perturbation density, axial velocity, radial velocity, tangential velocity and pressure, respectively, $\mathrm{D}_0/\mathrm{D}t \equiv \partial/\partial t + M_x \partial/\partial x$ and $M_x = U_x/c_{0m}$. Also, we recall that the mean pressure is assumed constant, with non-dimensional value equal to $1/\gamma$. In this section, we examine solutions to (3.9)–(3.13) to clarify the effects of the mean flow and suggest inflow conditions of interest for the nonlinear calculations.

3.2.1. *Modal analysis*

A simple class of solutions to the linearized Euler equations may be obtained in terms of eigenmodes. These eigenmode solutions display the different types of disturbances which exist and their characteristics. They are also useful for formulating inflow–outflow conditions (Atassi & Ali 2002; Atassi 2004) and studying the coupling of the modes (Atassi 2003) and their stability. The following Fourier expansion is assumed:

$$\begin{aligned}&\{\rho', u_x, u_r, u_\theta, p'\}(x, r, \theta; t)\\ &\quad = \int_{-\infty}^{\infty} \sum_{m=-\infty}^{\infty} \sum_{n=1}^{\infty} \{\rho_{mn}, X_{mn}(r), R_{mn}(r), T_{mn}(r), p_{mn}(r)\} \mathrm{e}^{\mathrm{i}(-\omega t + m\theta + k_{mn}x)}\, \mathrm{d}\omega,\end{aligned} \tag{3.14}$$

where m and n are integer modal numbers characterizing the circumferential and radial eigenmodes, respectively. The input parameters are the reduced frequency, $\omega = \Omega r_m / c_{0m}$ and the circumferential mode number m. Since the equations are linear, each Fourier component can be considered separately. Substituting (3.14) into the linearized Euler equations gives a coupled system of equations governing the eigenmodes,

$$\Lambda_{mn}\rho_{mn} - \frac{1}{r}\frac{\mathrm{d}}{\mathrm{d}r}[(\rho_0 r)(\mathrm{i}R_{mn})] + \rho_0\left(\frac{m}{r}T_{mn} + k_{mn}X_{mn}\right) = 0, \tag{3.15}$$

$$\rho_0\left(\Lambda_{mn}X_{mn} - \frac{\mathrm{d}M_x}{\mathrm{d}r}\mathrm{i}R_{mn}\right) + k_{mn}p_{mn} = 0, \tag{3.16}$$

$$\rho_0\Lambda_{mn}T_{mn} + \frac{m}{r}p_{mn} = 0, \tag{3.17}$$

$$\rho_0(\Lambda_{mn}\mathrm{i}R_{mn}) + \frac{\mathrm{d}p_{mn}}{\mathrm{d}r} = 0, \tag{3.18}$$

$$\Lambda_{mn}p_{mn} + \frac{m}{r}T_{mn} + k_{mn}X_{mn} - \mathrm{i}\frac{1}{r}\frac{\mathrm{d}}{\mathrm{d}r}(rR_{mn}) = 0, \tag{3.19}$$

where the convective eigenvalue Λ_{mn} is defined by the expression

$$\Lambda_{mn} = -\omega + k_{mn} M_x. \tag{3.20}$$

The boundary condition at the hub and tip radii is

$$R_{mn}(r) = 0. \tag{3.21}$$

The acoustic, vortical and entropic modes are coupled to each other through the mean-flow and density gradients. Discretizing the equations leads to an algebraic system of equations of the form

$$[A]z = k_{mn}[B]z, \tag{3.22}$$

where $[A]$ and $[B]$ are real matrices resulting from (3.15)–(3.19) and z is an eigenvector representing the eigenfunctions $\rho_{mn}, X_{mn}, T_{mn}, \mathrm{i}R_{mn}$ and p_{mn}. Solutions to (3.22) are obtained using the spectral method described in Golubev & Atassi (1998).

We first study the modal equations (3.15)–(3.19) to see whether there are pressure-free solutions which can be obtained without resorting to numerical methods. These solutions when expressed in terms of Fourier modes with a constant k^c_{mn} will restrict the value of r to r_c, for which $\Lambda_{mn} = 0$. The weak solutions are

$$p_{mn} = 0, \tag{3.23}$$

$$R_{mn} = 0, \tag{3.24}$$

$$X_{mn} = -\frac{m}{r_c k^c_{mn}} T_{mn}, \tag{3.25}$$

$$T_{mn} = A_{mn}\delta(r - r_c), \tag{3.26}$$

$$\rho_{mn} = B_{mn}\delta(r - r_c), \tag{3.27}$$

where $k^c_{mn} = \omega / M_x(r_c)$ and $\delta(r - r_c)$ is the Dirac delta function. Note that r_c will be in the interval, defined by $\Lambda_{mn} = 0$ for the given velocity profile, between hub and tip. Note also that the relationship between X_{mn} and T_{mn} implies that the solution is divergence free and ρ_{mn} is independent of the velocity. A superposition of the weak solutions (3.25)–(3.27) at the different radial locations of the duct yields

$$\{X_{mn}, T_{mn}, \rho_{mn}\} = \int_{r_h}^{r_t} \{f^X_{mn}(r_c), f^T_{mn}(r_c), f^\rho_{mn}(r_c)\}\delta(r - r_c)\mathrm{e}^{\mathrm{i}(k^c_{mn}x - \omega t + m\theta)}\,\mathrm{d}r_c \tag{3.28}$$

or

$$\{X_{mn}, T_{mn}, \rho_{mn}\} = \left\{f^X_{mn}(r), f^T_{mn}(r), f^\rho_{mn}(r)\right\}\mathrm{e}^{\mathrm{i}(\alpha_{mn}(r)x - \omega t + m\theta)} \tag{3.29}$$

where $\alpha_{mn}(r) = \omega / M_x(r)$. Equation (3.29) represents a special family of solutions which purely convect with the mean flow velocity. Note that for uniform mean flows such purely convected solutions always exist (Kovàsnznay 1953).

If $R_{mn} \neq 0$ and $\mathrm{d}M_x/\mathrm{d}r \neq 0$ then (3.16)–(3.19) show that it is not possible to find a pressure-free, $p_{mn} = 0$, solution. However, for $\mathrm{d}M_x/\mathrm{d}r = 0$, and $R_{mn} \neq 0$, (3.15)–(3.19) show that it is possible to find pressure-free purely convected solutions for the velocity, (X_{mn}, R_{mn}, T_{mn}). Multiplying (3.19) by ρ_0 and subtracting it from (3.15) gives

$$\Lambda_{mn}\rho_{mn} = \mathrm{i}\frac{\mathrm{d}\rho_0}{\mathrm{d}r} R_{mn}. \tag{3.30}$$

Since R_{mn} is different from zero, (3.30) shows that, as $\Lambda_{mn} \to 0$, ρ_{mn} must be singular at every point. This non-local non-integrable singular behaviour is in contrast with the solutions (3.23)–(3.27), which have a local and integrable singularity because R_{mn}

is equal to zero. This non-local non-integrable behaviour suggests an instability for the density. In § 3.3, we examine and demonstrate the existence of growing solutions for the density in the special case $\mathrm{d}M_x/\mathrm{d}r = 0$.

In the general case, $\mathrm{d}M_x/\mathrm{d}r \neq 0$ and $\mathrm{d}\rho_0/\mathrm{d}r \neq 0$, an unsteady pressure field is produced by the mean-flow gradients. To better understand the pressure field of the convected modes, (3.15)–(3.19) can be reduced to a generalized Pridmore–Brown equation (Vilenski & Rienstra 2005),

$$\frac{\mathrm{d}^2 p_{mn}}{\mathrm{d}r^2} + \left(\frac{1}{r} - \frac{2k_{mn}\mathrm{d}M_x/\mathrm{d}r}{\Lambda_{mn}} - \frac{\mathrm{d}(\log\rho_0)}{\mathrm{d}r}\right)\frac{\mathrm{d}p_{mn}}{\mathrm{d}r} + \left(\Lambda_{mn}^2\rho_0 - k_{mn}^2 - \frac{m^2}{r^2}\right)p_{mn} = 0, \tag{3.31}$$

where

$$\frac{\mathrm{d}p_{mn}}{\mathrm{d}r} = 0, \qquad r = r_h, r_t.$$

The two terms in (3.31) involving the mean density distinguish this equation from the conventional Pridmore–Brown equation derived for incompressible flow. The convective modes propagate with a phase speed close to that of the mean-flow speed $M_x(r)$, so the convective eigenvalue Λ_{mn} must be small for some radial position r. As a result, for moderate density gradients the term $2k_{mn}\Lambda_{mn}^{-1}\mathrm{d}M_x/\mathrm{d}r$ should be large compared with the mean density gradient, $\mathrm{d}\log(\rho_0)/\mathrm{d}r$, and thus it should characterize the stability of the solution.† In this case, the pressure field should be similar to the conventional Pridmore–Brown equation derived for incompressible parallel shear flows. The necessary condition for the stability of parallel shear flows is that the mean flow has an inflection point (Drazin & Reid 1984) and so the characteristics of the mean flow-velocity profile should play an important role in these instabilities.

In what follows, we compute numerical solutions for the modal equations. We consider reduced frequencies and azimuthal wavenumbers of order one. In this parameter space, the coupling between mean-flow gradients and unsteady perturbations may be strong and we examine the stability of the modes to see what effect the mean-temperature and velocity gradients have on the growth and decay of the disturbances.

We consider mean-density gradients caused by a non-uniform Gaussian temperature distribution which is hottest at the mean radius of the duct. The assumed density variation is

$$\rho_0(r) = 1 + \Delta\left[1 - \exp\left(-\frac{(r-1)^2}{\sigma^2}\right)\right], \tag{3.32}$$

where Δ and σ are constants corresponding to the amplitude and the width of the radial density non-uniformity, respectively.

We take the axial-velocity radial profile to be such that $\rho_0 M_x = K$ is constant, i.e.

$$M_x(r) = \frac{K}{1 + \Delta[1 - \exp(-(r-1)^2/\sigma^2)]}. \tag{3.33}$$

Thus, the axial velocity is not uniform and the mean flow contains vorticity in the azimuthal direction, (3.6). Figure 1(*a*, *b*) shows the non-dimensional mean velocity and density for $\rho_0 M_x = 0.2934$, $\Delta = 0.1875$ and $\sigma = 0.21$. Figure 1(*c*, *d*) shows the non-dimensional mean velocity and density for a medium Mach number case, which satisfies $\rho_0 M_x = 0.492$. Note that the mean density profile is identical to that in

---

† This argument was suggested by an anonymous referee.

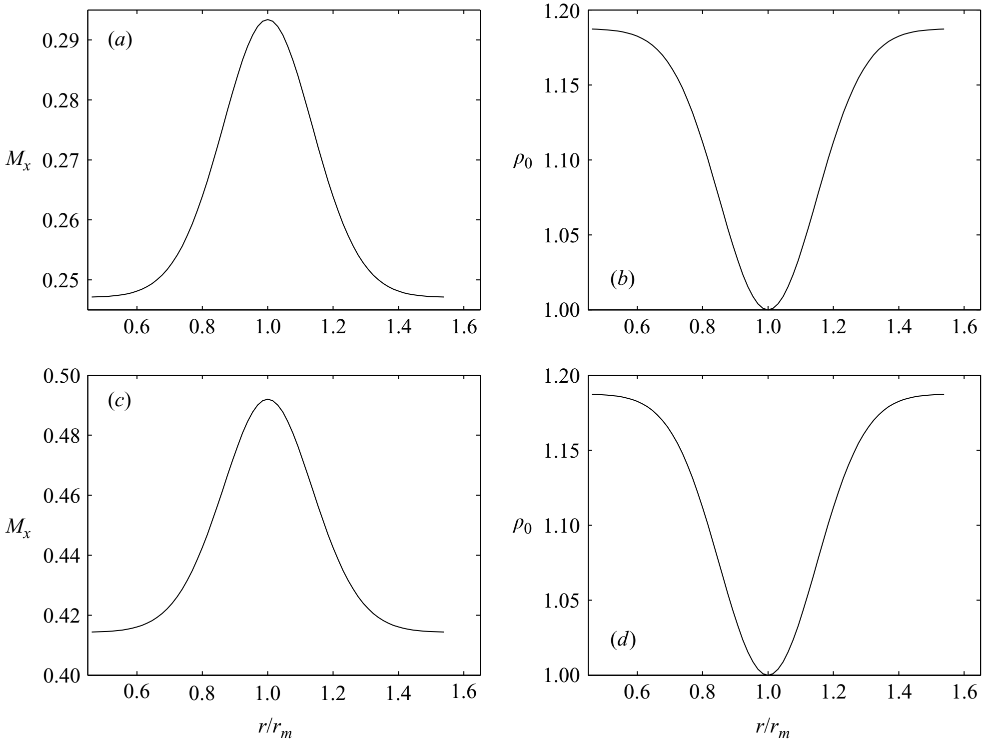

FIGURE 1. (a,b) Non-dimensional mean flow versus non-dimensional duct radius for a low-mach-number case: (a) axial velocity and (b) density. (c,d) As (a,b) but for a medium-mach-number case.

figure 1(b). The density and axial velocity change by nearly 20 per cent from the mean radius to the duct walls. The static pressure is constant from hub to tip. In order to examine the effect of the mean-density gradient, we also consider a case with a constant mean density and the same velocity distribution as that defined in (3.33), taking $K=0.2934$, $\Delta=0.1875$ and $\sigma=0.21$. We calculate the eigenmodes for an annular duct with hub–tip ratio 0.3, reduced frequency $\omega=1.0$, circumferential wavenumber $m=1$ and with the mean flow given in (3.32), (3.33) and shown in figure 1(a,b).

For a constant mean density, (3.15)–(3.19) have three possible families of solutions: (i) purely convected delta-type solutions as in (3.23)–(3.27) with $B_{mn}=0$; (ii) solutions that are hydrodynamically unstable owing due to the presence of inflection points (Drazin & Reid 1984) in the velocity profile (3.33); and (iii) stable solutions with non-zero pressure governed by the conventional Pridmore–Brown equation.

For a non-uniform density gradient, our previous analysis of the modal equations (3.15)–(3.19) suggests that there are again three possible families of solutions: (i) purely convected delta-type solutions as in (3.23)–(3.27); (ii) solutions that are hydrodynamically unstable owing to the presence of inflection points in the the velocity profile (3.33) which, except for the density eigenfunction, for the low Mach numbers considered should be practically independent of the mean-density profile; and (iii) stable solutions with non-zero pressure governed by the generalized Pridmore–Brown equation (3.31). Note that the effects of the mean-density profile on the density

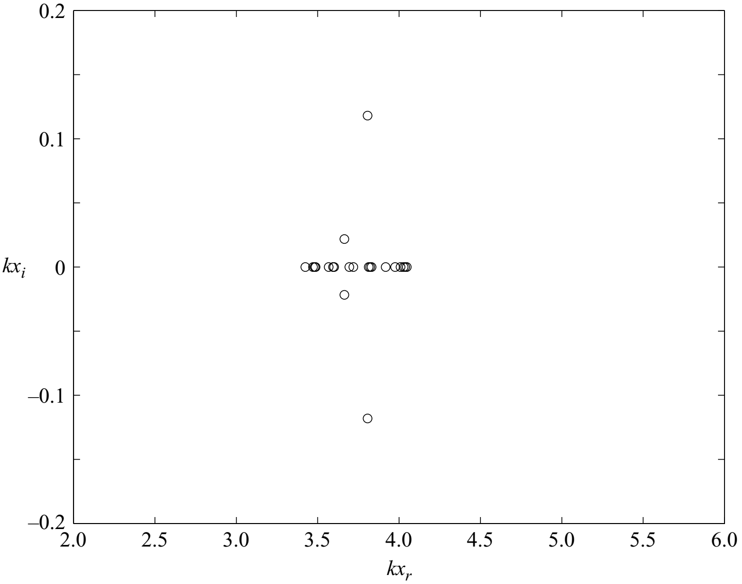

FIGURE 2. The eigenmodes which lie in the continuous spectrum $3.4 < k_{mn} < 4.1$ for the mean-flow profiles given in figure 1(*a*, *b*). The vertical and horizontal axes represent the imaginary and real parts of the axial wavenumber in the complex plane. The reduced frequency $\omega r_m / c_m$ is 1 and the circumferential wavenumber m is 1.

eigenfunction will be examined in more detail in the context of the full linearized equations, in particular, by solving the full nonlinear Euler equations numerically since these effects cannot be obtained by solution of the modal equations (3.15)–(3.19).

3.2.2. *Numerical modal solutions*

Figure 2 shows the distribution of mode spectra corresponding to the mean flow in figure 1(*a*, *b*), in terms of the wavenumber k_{mn} in the complex plane. The modes whose imaginary wavenumber is zero correspond to the purely convected modes and form the continuous spectrum whose eigenvalues extend from $\omega/\max M_x < k_{mn} < \omega/\min M_x$. Note that there are two unstable modes. The complex wavenumbers of the unstable modes with the mean-flow profile shown in figure 1(*a*) are $k_{mn} = (3.807, -0.118)$ and $k_{mn} = (3.65, -0.029)$. As noted above, these unstable modes are associated with the inflection points in the velocity profile and are nearly independent of the density profile. If we make the density uniform, the eigenvalues of the two unstable modes become $k_{mn} = (3.794, -0.122)$ and $k_{mn} = (3.63, -0.029)$ respectively. Furthermore, if we change the mean-velocity profile from a Gaussian to a parabolic profile, i.e. a velocity profile that does not have an inflection point, the unstable modes disappear. Increasing the Mach number, as in figure 1(*c*) but maintaining the Gaussian profile, alters the wavenumber but two unstable modes are still present. Figure 3 shows the eigenfunctions of one of the neutrally stable modes lying in the continuous spectrum. The solution corresponds to the delta-function-type solutions found analytically in the previous section. Although a delta-type solution is difficult to capture numerically, our numerical scheme is accurate enough to resolve them, as shown in figure 3. The left-hand panel shows all three components of the velocity and the pressure while the right-hand panel shows the density. As expected, the purely convected mode is zero everywhere

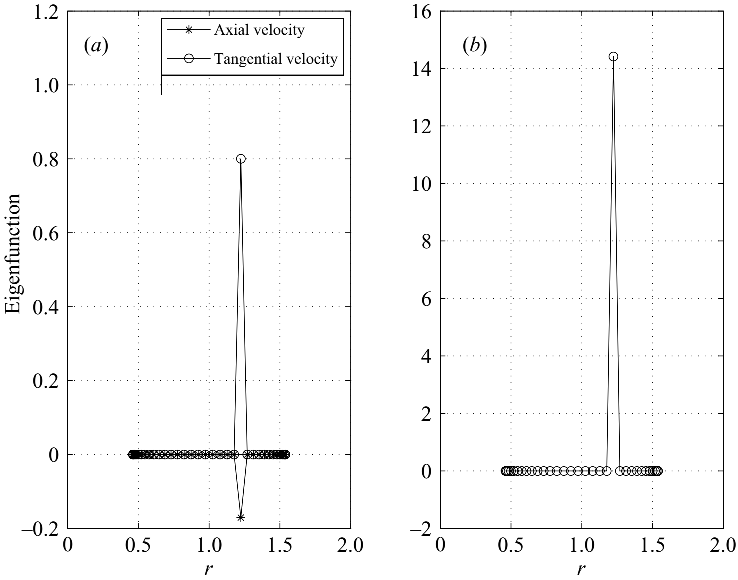

FIGURE 3. (*a*) The eigenfunctions for one of the modes in the continuous spectrum vs. the radius. The axial and tangential eigenfunctions are each non-zero at a single point. They are purely convected at this radial location. The tangential and axial wavenumbers are $m=1$, $k_{mn}=3.832$, and the axial and tangential velocities satisfy the divergence-free condition. The pressure and radial eigenfunctions are zero. (*b*) The density eigenfunction.

except at a single radius, the critical radius $r=r_c$. Here the numerical solution shows a singular, delta-function-type, solution in agreement with the analytical solution given in (3.23)–(3.27). Note that u_x and u_θ are connected by the divergence-free condition. Observe that the mode lies at $r=r_c=1.224$ with axial wavenumber $k_{mn}=3.832$ and that the relationship between the axial and tangential velocities satisfy $\nabla\cdot\boldsymbol{u}=0$ or

$$T_{mn}=-\frac{k_{mn}r_c}{m}X_{mn}.$$

Precisely, the numerical results give $X_{mn}=-0.1706$ and $T_{mn}=0.8$, which satisfy the divergence-free condition. The radial velocity and pressure are identically zero, also in agreement with the analytical results.

Another set of modes which lie in the continuous spectrum are the entropy modes. These modes have zero velocity and pressure and are associated with pure density fluctuations. They lie in the continuous spectrum with zero imaginary part, indicating that all the entropy modes are neutrally stable. Again, the eigenfunction of the purely convected mode is zero everywhere except at the critical radius $r=r_c$ where the numerical solution shows a singular delta-function-type solution in agreement with the analytical solution given in (3.27). The entropy modes contain a spectrum with phase velocity equal to the local mean velocity, like the velocity modes shown in figure 2. Thus without examining the eigenfunctions it is difficult to distinguish the entropy-dominated and vorticity-dominated modes.

In figure 4, we plot the complex eigenfunctions of the most unstable mode for both a uniform and a non-uniform density profile, with the mean-velocity profile shown in figure 1(*a*). The dashed lines correspond to the eigenfunctions for a mean flow without mean-density gradients and the solid lines denote the eigenfunctions

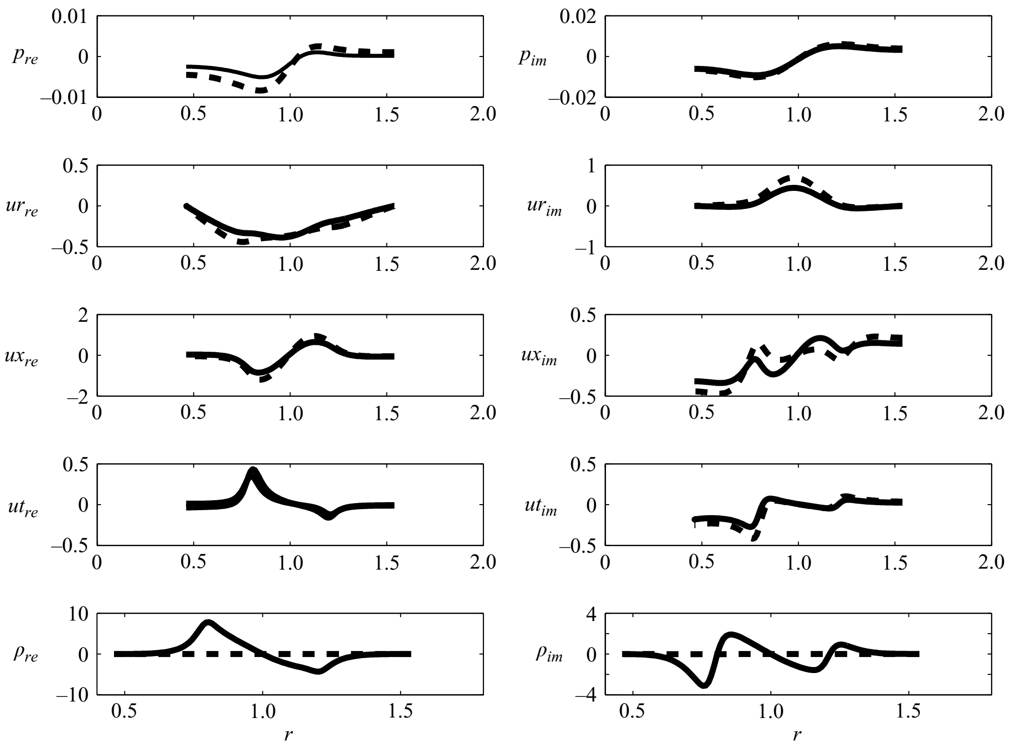

FIGURE 4. The real and imaginary parts of the eigenfunctions corresponding to the most unstable mode for two different mean flows. The eigenfunctions denoted by solid lines correspond to the eigenfunction for the mean velocity given in figure 1(*a*) and the density profile given in figure 1(*b*). The eigenfunctions denoted by the dashed lines are the solution associated with the constant mean-density profile. The largest difference between the two solutions is visible in the density, which is much larger for the nonzero-density-gradient case than for the zero-density-gradient case.

for a mean flow with density gradients. The difference between the eigenfunctions is very small except for the density eigenfunction, which is plotted in the fifth row: the density eigenfunction for the non-uniform-density case is very large compared with the pressure perturbation while the uniform-density case has a density eigenfunction which is equal to the pressure eigenfunction. The reason is that the density eigenfunction is inversely proportional to Λ_{mn}, which lies between 0.1 and 0.2 for the unstable mode. The velocity field shown in figure 4 shows that all three velocity components of the unstable mode are significant.

The instability behaviour of the two unstable modes in figure 2 depends strongly on the circumferential wavenumbers. For larger circumferential modes, $m = 8$, a much smaller growth rate for the most unstable mode occurs, and if we further increase the circumferential wavenumber to $m = 10$ then no unstable modes occur, suggesting that the hydrodynamic exponential instability is stabilized by larger circumferential wavenumbers.

3.3. *Algebraically growing pressure-free solutions due to mean-density gradients*

In this section, we derive axially evolving pressure-free solutions and distinguish the effect of the density gradients from those of the velocity gradients by considering a mean flow with uniform velocity. When the mean flow velocity is uniform, the linearized equations (3.9)–(3.13) reduce to

$$\frac{\mathrm{D}_0}{\mathrm{D}t}\rho' + \rho_0 \nabla\cdot\boldsymbol{u} + \frac{\mathrm{d}\rho_0}{\mathrm{d}r}u_r = 0, \tag{3.34}$$

$$\frac{\mathrm{D}_0}{\mathrm{D}t}\boldsymbol{u} = -\frac{\nabla p'}{\rho_0}, \tag{3.35}$$

$$\frac{\mathrm{D}_0}{\mathrm{D}t}p' + \nabla\cdot\boldsymbol{u} = 0. \tag{3.36}$$

Note that (3.35), (3.36) are independent of ρ'; however, ρ', governed by (3.34), depends on $\boldsymbol{u}$. Equations (3.35), (3.36) have the following solution:

$$p' = 0, \tag{3.37}$$

$$\boldsymbol{u} = \boldsymbol{u}(x - M_x t\boldsymbol{e}_x,\ r,\ \theta), \tag{3.38}$$

with the condition that the disturbance velocity is solenoidal. Note that if we impose a divergence-free $\boldsymbol{u}$ at the inlet (x_0, t_0) then the velocity $\boldsymbol{u}$ defined by (3.38) will always be solenoidal. Thus, (3.34) reduces to

$$\frac{\mathrm{D}_0}{\mathrm{D}t}\rho' + \frac{\mathrm{d}\rho_0}{\mathrm{d}r}u_r(x - M_x t\boldsymbol{e}_x, r, \theta) = 0. \tag{3.39}$$

This equation can be readily integrated and has the solution

$$\rho' = \rho^*(\boldsymbol{x} - U_x t\boldsymbol{e}_x,\ r,\ \theta) - \frac{x}{M_x}\frac{\mathrm{d}\rho_0}{\mathrm{d}r}u_r(x - M_x t\boldsymbol{e}_x,\ r,\ \theta). \tag{3.40}$$

This case clearly shows that it is possible to have an algebraically growing density fluctuation driven by the density gradients in the flow. The velocity field, however, convects independently of the density downstream, with the uniform flow without growth in its amplitude.

The above solution shows a linear growth in the density perturbation due to coupling between the mean-density gradient and the radial-velocity perturbation as the wave propagates downstream. Algebraic growth in time due to the interaction of mean-flow gradients with a time-independent transverse-velocity perturbation has been conjectured to be important in the formation of long streaky structures in turbulent shear flows (Landahl 1980). In this case, the evolution of the initial disturbances in time was studied. Ellingsen & Palm (1975) and, later, Hanifi & Henningson (1998) concluded that perturbations which are independent of the streamwise coordinate x will increase linearly with time. Landahl (1980) extended the results of Ellingsen & Palm and showed that initial conditions lead to a growth in the kinetic energy in time associated with the linear growth in time of the streamwise extent of the disturbance. This occurs even when the disturbance velocities do not grow.

4. Nonlinear evolution of incident vortical and entropic disturbances

In this section, we compute the nonlinear evolution and examine the stability of various incident disturbances. We look first at the effect of the mean-flow gradients and the form of the incident disturbance on the propagation of the vortical and entropic disturbances to see whether the calculations are consistent with the linear analysis. Then we increase the amplitude of the inlet excitation to see how nonlinear effects alter the propagation of the incident time-harmonic waves.

4.1. *Incident disturbance representation*

In what follows, we present the incident disturbance representation at the inlet of the computational domain. To highlight the effect of the density gradients on the solution, we follow the disturbance representation given in Atassi, H. M. *et al.* (2004) for time-harmonic vortical disturbances in a non-uniform flow. In that work, the authors modelled the interaction of wakes shed from a fan with structural struts, using the isentropic linearized Euler equations. Based on the Fourier decomposition of fan wakes from Reynolds-averaged Navier–Stokes calculations, the authors observed that the axial pressure gradient and density of the wake harmonics are small compared with the velocity fluctuations. They then eliminated the axial derivatives from the axial-velocity to obtain a relationship between the axial-velocity perturbation and the radial- and circumferential-velocity perturbations, which were given. Although the current paper solves the nonlinear Euler equations, we locally linearize at the inflow boundary and thus we can use the incident-vortical-wave representation based on the linearized Euler equations. We briefly give details of the inflow representation below.

Linearizing the energy and axial-momentum equations we obtain

$$\nabla \cdot \boldsymbol{u} = -\frac{\mathrm{D}_0 p'}{\mathrm{D}t}, \tag{4.1}$$

$$\frac{\mathrm{D}_0}{\mathrm{D}t} u_x + u_r \frac{\mathrm{d}M_x(r)}{\mathrm{d}r} = -\frac{1}{\rho_0}\frac{\partial p'}{\partial x}. \tag{4.2}$$

We impose a vortical disturbance for which $u_\theta = u_\theta^{(v)}$ and $u_r = u_r^{(v)}$ are assumed known and $\partial p^{(v)'}/\partial x$ and $\mathrm{D}_0 p^{(v)'}/\mathrm{D}t$ are small. Then multiplying (4.1) by M_x, we eliminate $\partial u_x^{(v)}/\partial x$ by subtracting the linearized continuity equation from the x-momentum equation and obtain

$$\frac{\partial u_x^{(v)}}{\partial t} - \frac{M_x^2}{r}\frac{\partial}{\partial r}\left(\frac{r u_r^{(v)}}{M_x}\right) - \frac{M_x}{r}\frac{\partial u_\theta^{(v)}}{\partial \theta} = 0. \tag{4.3}$$

Note that this expression reduces to that given in Atassi, H. M. *et al.* (2004) in the limit of zero mean swirl. Thus, by specifying the tangential and radial components of the velocity we can specify incident vortical disturbances.

Owing to the periodicity of the problem in θ we can, without loss of generality, expand the inlet velocity and density in terms of a Fourier series,

$$\boldsymbol{u} = \sum_{m_g=-\infty}^{m_g=+\infty} \hat{\boldsymbol{u}}_{m_g}(x_i, r)\, \mathrm{e}^{\mathrm{i}(m_g\theta - \omega t)}, \tag{4.4}$$

$$\rho' = \sum_{m_g=-\infty}^{m_g=+\infty} \rho_{m_g}(x_i, r)\, \mathrm{e}^{\mathrm{i}(m_g\theta - \omega t)}. \tag{4.5}$$

Note that the radial velocity $\hat{u}_{rm_g}(r)$ must satisfy the impermeability condition at the hub and the tip.

4.2. *Outflow boundary condition*

At the outflow boundary, we again locally linearize and write non-reflecting boundary conditions for the perturbation pressure, as in Atassi, O. V. & Galan (2005), and the axial velocity not induced by the acoustic pressure field is given by the pure-convection condition,

$$\frac{\mathrm{D}u_x^{(v)}}{\mathrm{D}t}=0. \tag{4.6}$$

4.3. *Numerical results: evolution of entropically and vortically dominated disturbances*

In this section, we solve the Euler equations to examine the effect of (i) the mean-flow profile, (ii) the azimuthal wavenumber and (iii) the initial amplitude of the disturbance on the evolution of incident vortical disturbances. We first consider two simple validation cases: a pure density fluctuation and a vortical disturbance with a uniform mean velocity but non-uniform density profile. In the first case the velocity perturbation is zero, so no coupling between the velocity and density fluctuation occurs and a simple purely convected solution for the density perturbation exists and in the second case, an analytic solution showing algebraic growth in the density fluctuation was derived in § 3.3. We then consider a vortical excitation with non-uniform density and velocity profiles for which coupling between both the velocity and the density fluctuations occurs and examine the effect of azimuthal wavenumber on the disturbance evolution. While eigenmode solutions were given for a non-uniform mean velocity and density profile in § 3.2, in what follows we solve the nonlinear Euler equations as an initial-value problem. These solutions should highlight the limitations of solving the eigenvalue problem. For example, owing to the complexity of the mean flow the eigenvalue problem is not Sturm–Liouville and so completeness of the solutions cannot be proven. Moreover, owing to the assumed form of the eigenmode solution with constant axial wavenumber a continuous spectrum of modes exists in the eigenmode solution.

In what follows, we consider reduced frequencies equal to unity in a constant-area annular duct with hub–tip ratio 0.3 and the mean velocity and density given in figure 1(*c*, *d*). Recall that the eigenmode analysis in the low-frequency regime of interest, $\omega r_m/c_{0m}=1$, showed that the most unstable modes occur for small azimuthal wavenumbers. This is expected because in this parameter space the wavelength of the incident disturbances is of the order of the mean radius of the duct. As a result, the disturbances vary on the same scale as the mean flow and the strongest coupling between the mean-flow gradients and the disturbances is expected to occur.

4.3.1. *Evolution of an entropic wave*

The incident-density fluctuation at the inlet of the computational domain is given by

$$\rho'=a\exp[\mathrm{i}(m\theta-\omega t)], \tag{4.7}$$

with non-dimensional amplitude $a=1\times10^{-3}$, circumferential wavenumber $m=1$ and zero velocity and pressure perturbation. This problem has the analytic solution

$$\left.\begin{aligned}\rho'&=a\exp\left[\mathrm{i}\left(\frac{\omega}{M_x(r)}x+m\theta-\omega t\right)\right],\\ \boldsymbol{u}&=0,\\ p'&=0.\end{aligned}\right\} \tag{4.8}$$

Owing to the difference in Mach number across the radius of the duct, lines of constant phase will have a Gaussian shape like that of the mean flow and the axial shift between the hub of the duct and the mean radius, where the Mach number is a

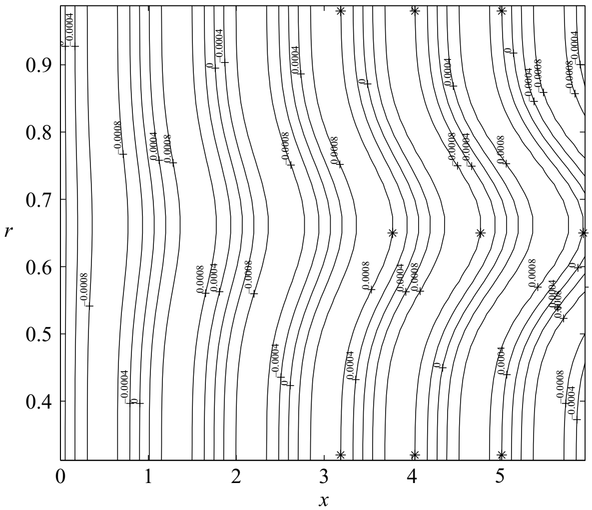

FIGURE 5. Contours of constant-density fluctuation are shown for a constant-θ or (x, r)-plane of the duct at an instant in time. The dimensionless frequency of the excitation is $\omega r_m/c_0 = 1.0$ and the circumferential wavenumber is $m = 1$. The hub–tip ratio of the duct is 0.3.

maximum, is given by

$$\delta x = \frac{M_x(r_m) - M_x(r_h)}{M_x(r_m)} x = 0.185x,$$

where $x = 0$ is the inlet of the computational domain. In figure 5, we see a plot of the density perturbation at an instant in time where the solution has converged to a periodic solution with the same reduced frequency as the inlet excitation, ω. Near the centreline, the wave propagates with a wavelength λ equal to U/f where $f = \omega/(2\pi)$ is the frequency of the inlet excitation and U is the local axial velocity, which varies from hub to tip. Although the inlet excitation does not vary radially, the disturbance shows significant radial variation near the exit of the computational domain. As expected this results because the wave propagates with the local mean axial velocity, which is largest at the centreline of the duct. To compare the numerical solution and the analytical solution, the axial variation of a line of constant phase at three different locations is marked on figure 5 at $r = 0.32, 0.65, 0.98$ by a star symbol, using the exact solution given above. Excellent agreement between the numerical results and the exact solution is shown. The amplitude of the wave remains constant as the entropy disturbance convects downstream and the velocity and pressure components remain near zero, suggesting, also in agreement with the eigenmode results, that the coupling between entropy and vorticity is negligible when the radial velocity is zero and that the wave is neutrally stable.

4.3.2. *Evolution of entropic and vorticity disturbances in a flow with uniform velocity*

In this subsection, we assume a uniform mean-velocity profile with a radially varying mean-density profile as in figure 1(*d*). We then compare our results with the exact solution, (3.40), which shows that even without gradients in the mean-velocity profile the density perturbation grows linearly as it propagates downstream.

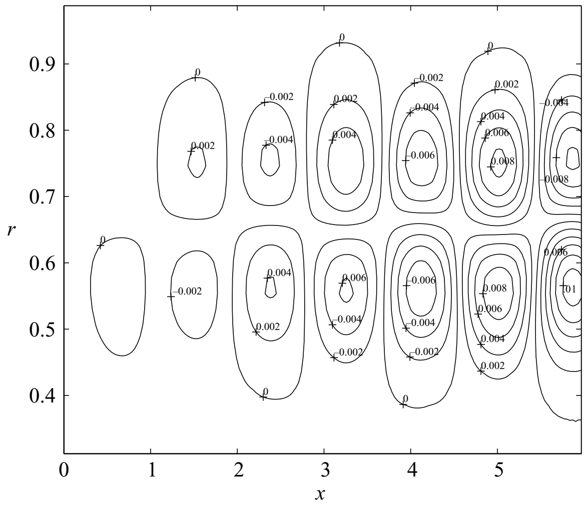

FIGURE 6. Contours of constant-density fluctuation are shown for a constant-θ or (x, r)-plane of the duct at an instant in time. The dimensionless frequency of the excitation is $\omega r_m/c_0 = 1.0$ and the circumferential wavenumber is $m = 1$. The hub–tip ratio of the duct is 0.3. The mean flow velocity is uniform and the density profile is given in figure 1(*d*).

The vortically dominated time-harmonic disturbance at the inlet has tangential and radial velocity components given by

$$\left.\begin{aligned} u_\theta &= aM_x \exp[\mathrm{i}(m\theta - \omega t)] \\ u_r &= \frac{a}{2}\sin\left(\pi\frac{r - r_h}{r_t - r_h}\right)\exp[\mathrm{i}(m\theta - \omega t)]. \end{aligned}\right\} \tag{4.9}$$

The axial velocity is given by (4.3). The pressure perturbation is zero and the density fluctuation, which is small, is produced by the mean-density gradients and the disturbance radial-velocity field. The amplitude is $a = 1 \times 10^{-3}$, the reduced frequency is $\omega = 1$ and the azimuthal order is $m = 1$.

Figure 6 shows a contour plot of the density fluctuation in the (x, r)-plane. As the wave propagates into the domain, the amplitude of the contours of constant density increases markedly in the mid-radius region where the density gradients are the largest. Close to the hub and tip of the duct, where the mean-density gradients are small, the amplitude of the density fluctuations is also small. The growing oscillations are nearly antisymmetric with respect to the mean radius of the duct. Recall that the mean radius is the location where the mean slope of the mean density changes from positive to negative.

For a better comparison of the numerical results and the linear theory, in figure 7 we show the evolution of the density with a line plot at the radial locations $r = 0.55$ and $r = 0.75$. Figure 7(*a*) shows the real part of the density as a function of x at an instant in time. The solid lines comprising the wave envelope reveal the linear change in amplitude that occurs as the wave propagates downstream, in agreement with the analytical results of § 3.3. In this case, the density fluctuations are coupled to the velocity field by the radial velocity and the mean-density gradients, but the velocity fluctuations are independent of the density profile since the mean velocity is uniform and the perturbation velocity is divergence free. Figure 7(*b*) shows the amplitude of the density as a function of x for $r = 0.75$. The solid line denotes the analytical

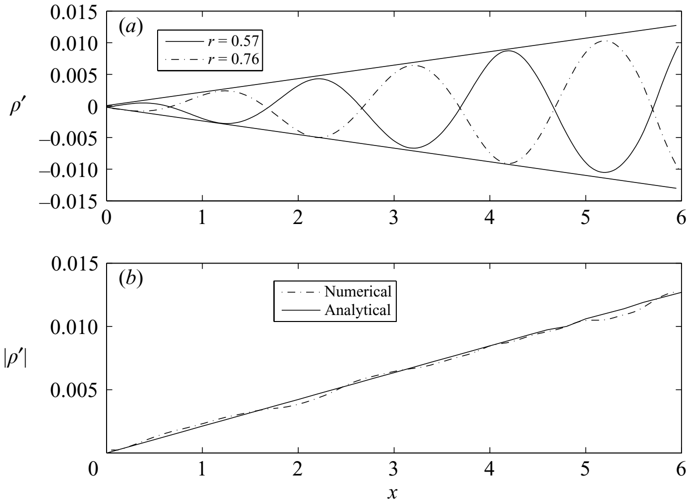

FIGURE 7. (*a*) A line plot of the density fluctuation as it propagates down the duct. The plot is shown at two radial locations, $r = 0.55$ and $r = 0.75$, at a constant-θ location of the duct at an instant in time. The dimensionless frequency of the excitation is $\omega r_m/c_0 = 1.0$ and the circumferential wavenumber is $m = 1$. The hub–tip ratio of the duct is 0.3. The mean flow velocity is uniform and the density profile is given in figure 1(*d*). (*b*) The amplitude of the wave vs. the analytical solution. The solid and dashed lines show the linear increase in amplitude from the analytical and numerical solutions, respectively, as the density fluctuation evolves downstream.

solution in (3.40) and the dashed line denotes the numerical solution. Again good agreement exists between the numerical and analytical solutions.

4.3.3. *Evolution of vorticity disturbances: effect of azimuthal wavenumber*

In this section, we revisit the mean flow shown in figure 1(*c*). Recall that the density is radially non-uniform with a Gaussian profile and that the mean velocity is also non-uniform with an inflection point and is chosen such that $\rho_0 M_x$ is constant. In what follows, we present numerical solutions of the Euler equations for incident disturbances with various azimuthal wavenumbers $m = 1, 8, 10$. Recall that for $m = 1$ there were two exponentially unstable modes while for $m = 8$ there was one exponentially unstable mode with a much smaller growth rate. The $m = 10$ case was found to be stable by the eigenmode analysis given in § 3.2.2.

The inlet excitation is a vortically–dominated disturbance with tangential and radial velocity components given by

$$\left.\begin{aligned} u_\theta &= aM_x(r)\exp[\mathrm{i}(m\theta - \omega t)],\\ u_r &= \frac{a}{2}\sin\left[\pi\left(\frac{r - r_h}{r_t - r_h}\right)\right]\exp[\mathrm{i}(m\theta - \omega t)]. \end{aligned}\right\} \qquad (4.10)$$

The axial velocity and the density field produced by the mean-density gradients and the radial velocity field are given by (4.3). The amplitude is $a = 1 \times 10^{-3}$, the reduced frequency is $\omega = 1$ and the azimuthal order is $m = 1$. For this azimuthal wavenumber, on the basis of the linear analysis we expect both algebraic and exponential instabilities to occur. In order to distinguish the type of instability, exponential or algebraic, we extend the computational domain to $x = (0, 12)$.

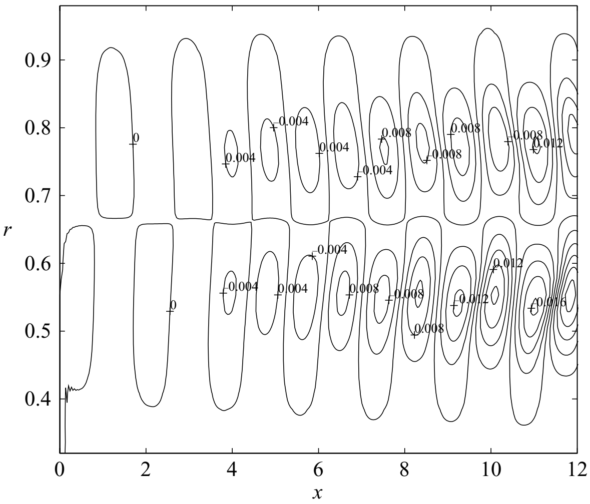

Figure 8. Contours of constant-density perturbation are shown for a constant-θ or (x, r)-plane of the duct at an instant in time. The dimensionless frequency of the excitation is $\omega r_m/c_0 = 1.0$ and the circumferential wavenumber is $m = 1$. The hub–tip ratio of the duct is 0.3. The mean flow is given in figure 1(*b*).

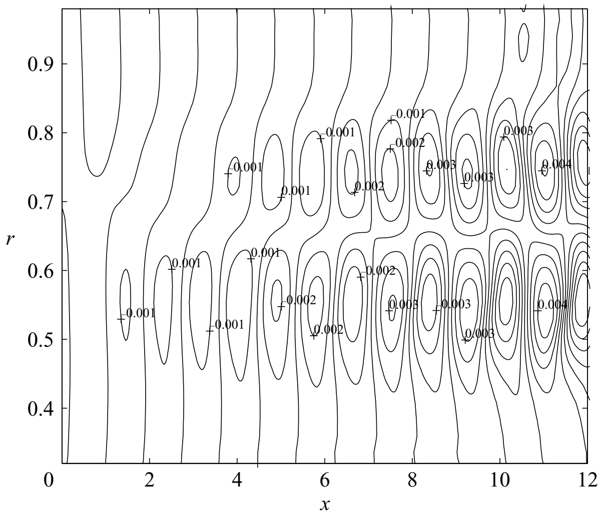

Figure 9. As figure 8 but showing contours of constant-axial-velocity perturbation.

Figures 8–10 show contours in the (x, r)-plane of the density, axial-velocity and radial-velocity perturbations, respectively. In figure 8, the density perturbation is nearly zero near the inlet. As the wave moves downstream, the amplitude of the density fluctuations grows to nearly 0.02. On both sides of the mean-radius location, positive and negative values of the density fluctuations are shown. Note that the effect of the mean velocity is that the shape of the density contours is no longer antisymmetric with respect to the mean-radius location. However, the scale of the density fluctuation at $x = 6$ is similar to that for the uniform mean-velocity case.

Figure 9 shows contours of the axial-velocity component. As the wave propagates downstream, concentrated regions with growing amplitude develop around the

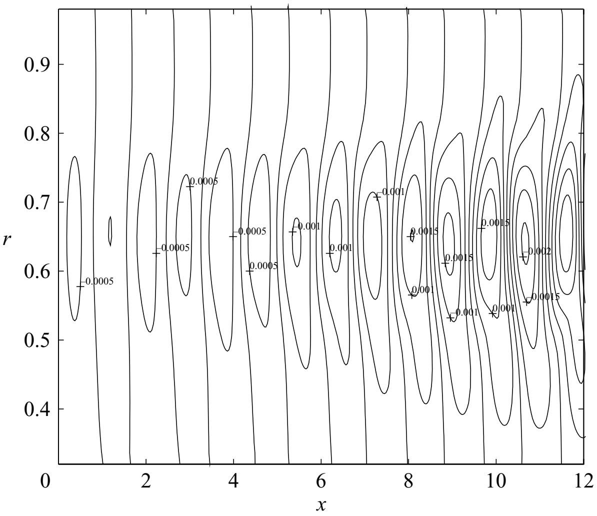

FIGURE 10. As figure 8 but showing contours of constant-radial-velocity perturbation.

mean-radius location. Closer to the hub and tip of the duct, where the mean-flow gradients are small, the growth of the waves is less visible and the wave convects downstream with a nearly constant amplitude.

Figure 10 shows an (x, r)-plane view of the radial-velocity component. Note that to satisfy the impermeability condition at the hub and the tip, the radial velocity goes to zero. The radial velocity also grows by a factor of nearly 5 between the inlet and the exit of the duct. The growth in amplitude of the incident wave and its associated increase in kinetic energy suggest that the wave is exponentially unstable owing to the mean-flow velocity gradient which has an inflection point in its radial profile.

To distinguish the type of growth more clearly, in figure 11 we show plots of the density, axial-velocity and radial-velocity perturbations. Figure 11(*a*) shows at an instant in time the density perturbation as it propagates downstream. The solid and dashed curves denote the density perturbation at the constant radial locations $r = 0.55$ and $r = 0.75$, respectively. Linear fits to the amplitude of the wave have been made to visualize the extent to which the solution deviates from linear growth. This shows that the growth is linear up to about $x = 5$. Downstream of this distance, the growth is faster than linear. Figures 11(*b*) and 11(*c*) show plots of the axial- and radial-velocity perturbations along two lines of constant radius, $r = 0.55$ (solid curve) and $r = 0.75$ (dashed curve). The growth is clearly not linear and an exponential fit of the growth along the line $r = 0.55$ is denoted by the solid envelope curve. The growth rate of this exponential fit is 0.14. It is of interest to compare this with the growth rate of the most unstable mode predicted by an eigenmode analysis of the mean flow in figure 1(*c, d*). Since the modal analysis is scaled by the mean radius, $r_m = 0.65$, we rescale the imaginary part of the axial wavenumber by the tip radius, $1/r_m$, and obtain a growth rate of 0.13, which is slightly lower than that given by the numerical solution of the Euler equations. The plots show that far enough downstream the velocity perturbations are dominated by exponential growth. Furthermore, exponential growth in the radial velocity results in the superlinear growth observed in the density perturbation for $x > 6$ and shows the effects of the coupling between the density and velocity perturbations. We expect that, owing to

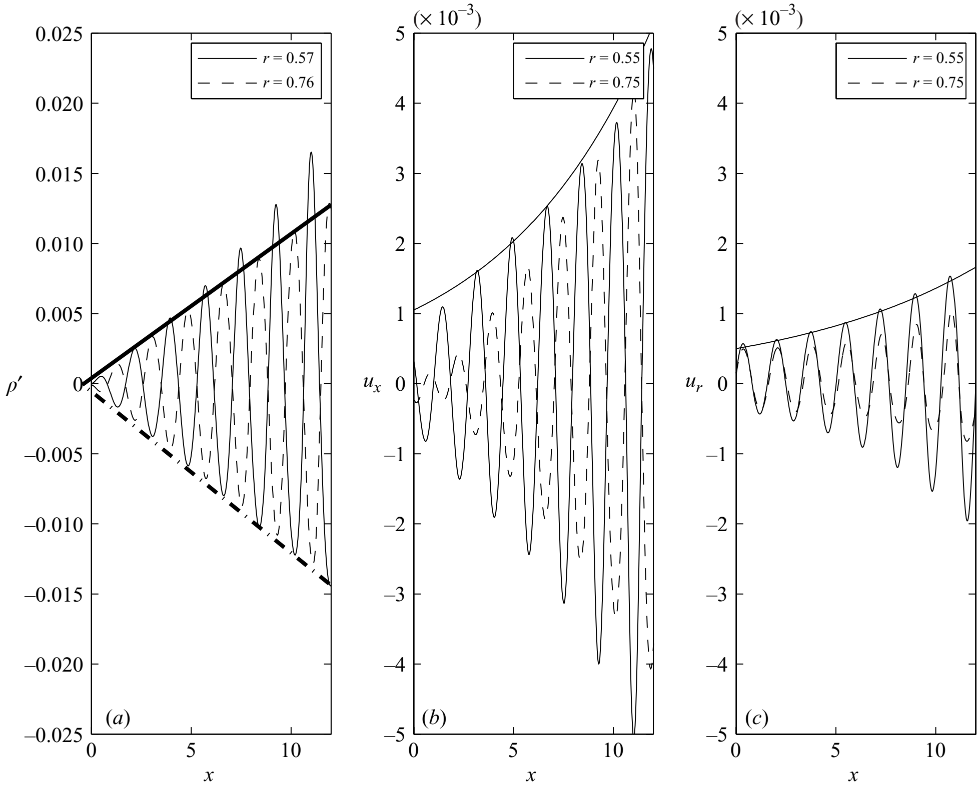

FIGURE 11. (*a*) The density perturbation along a line of constant radius at in instant in time. The solid curve is along $r = 0.55$ and the dashed curve is along $r = 0.75$. (*b*) The axial-velocity perturbation along a line of constant radius at an instant in time. The solid curve is along $r = 0.55$ and the dashed curve is along $r = 0.75$. (*c*) The radial-velocity perturbation along a line of constant radius at an instant in time. The solid curve is along $r = 0.55$ and the dashed curve is along $r = 0.75$. The dimensionless frequency of the excitation is $\omega r_m/c_0 = 1.0$ and the circumferential wavenumber is $m = 1$. The hub–tip ratio of the duct is 0.3.

this coupling, sufficiently far downstream the growth in the density perturbation will become exponential like that of the velocity perturbation.

Figures 12, 13 show the evolution of the density and axial-velocity perturbations for the $m = 8$ case. The magnitude of the density contours in figure 12 show the growth in the density perturbation as the wave propagates downstream. However, unlike the $m = 1$ case, the magnitude of the density is no longer nearly symmetric about the mean radius. Instead, the magnitude of the density fluctuations are larger above the mean radius than below it. The reason is that the asymmetric terms in the Euler equations containing the coefficient $(1/r)\partial/\partial\theta$ become more significant as m becomes larger and the radial-velocity perturbation becomes asymmetric with respect to the mean radius. Since the radial velocity is what drives the growth of the density, the growth in amplitude of the density becomes asymmetric. Contours of the axial-velocity fluctuation are shown in figure 13. The amplitude of the axial velocity increases slightly near the mean radius of the duct and the gradients in the velocity concentrate in the $0.5 < r < 0.7$ region. However, the rate of growth in the axial velocity is diminished from the $m = 1$ case and the growth is concentrated in a smaller

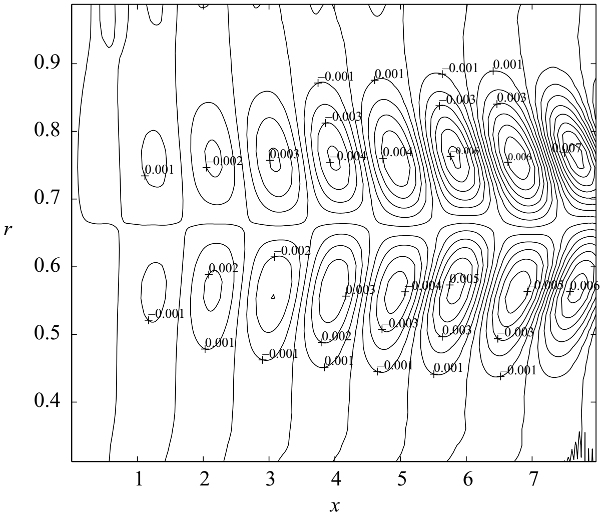

FIGURE 12. Contours of constant-density perturbation are shown for a constant-θ or (x, r)-plane of the duct at an instant in time. The dimensionless frequency of the excitation is $\omega r_m/c_0 = 1.0$ and the circumferential wavenumber is $m = 8$. The hub–tip ratio of the duct is 0.3.

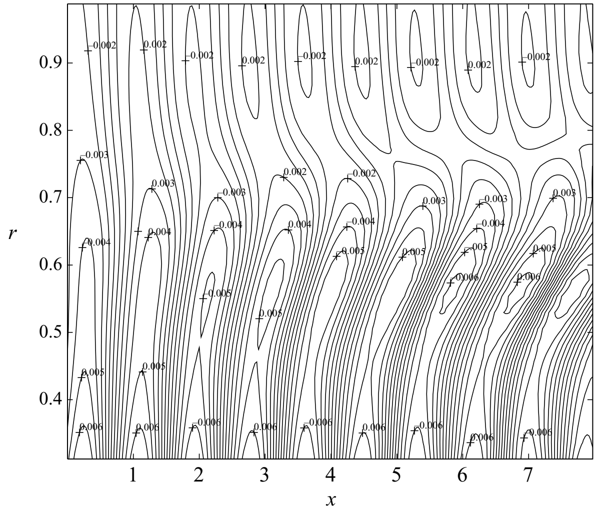

FIGURE 13. As figure 12 but showing contours of constant-axial-velocity perturbation.

radial swathe. This is in agreement with the normal-mode analysis, which found that the hydrodynamic instability is stabilized as the azimuthal wavenumber increases.

In figures 14, 15 there are contour plots of density and axial-velocity fluctuations with azimuthal wavenumber $m = 10$; this case, according to the eigenmode analysis in § 3, no longer exhibits instability. The density fluctuation shown in figure 14 grows as the wave propagates downstream, similarly to the $m = 8$ case where the growth is more rapid above the mean radius than below it. To understand this asymmetry in the growth we plot the radial-velocity contours in figure 16; these play the key role in coupling the perturbations to the mean flow. As the wave propagates downstream, the radial velocity has its largest magnitude above the mean radius. This

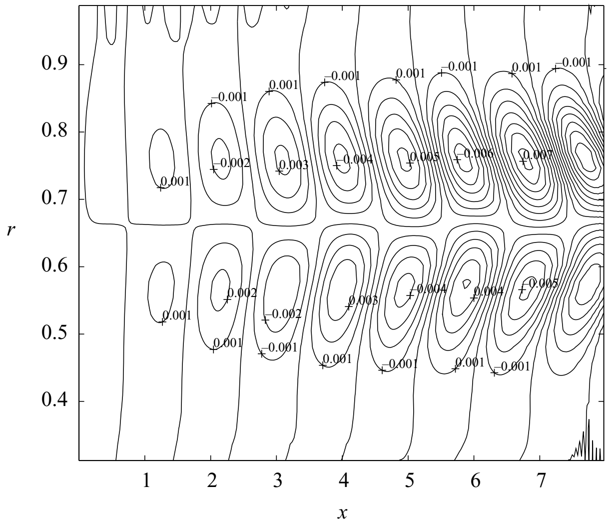

Figure 14. Contours of constant-density perturbation are shown for a constant-θ or (x, r)-plane of the duct at an instant in time. The dimensionless frequency of the excitation is $\omega r_m/c_0 = 1.0$ and the circumferential wavenumber is $m = 10$. The hub–tip ratio of the duct is 0.3.

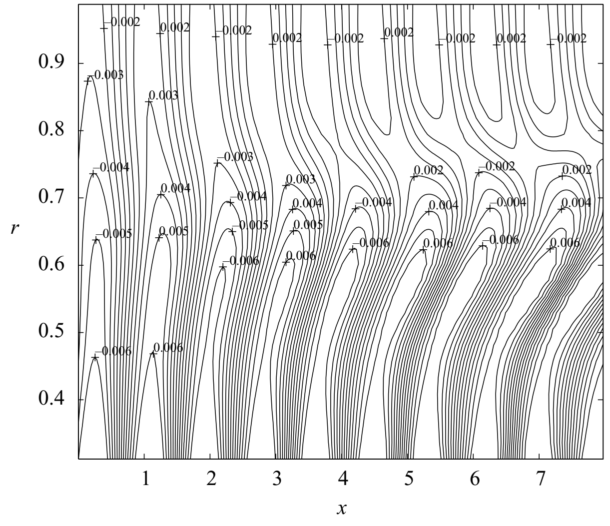

Figure 15. As figure 14 but showing contours of constant-axial-velocity perturbation.

result illustrates the importance of the coupling between the vortical velocity and the density perturbations since it relates the alteration in the radial-velocity to the evolution of the density perturbation.

Figure 15 shows contours of constant axial-velocity. The axial-velocity profile redistributes as the wave propagates downstream and shows concentrated regions at mid-radius, where the mean-flow gradients are significant. In the mid-radius region $0.5 < r < 0.6$ some growth in the contours is visible up to the axial location $x = 4$; however, beyond this the amplitude of the contours does not noticeably increase. In

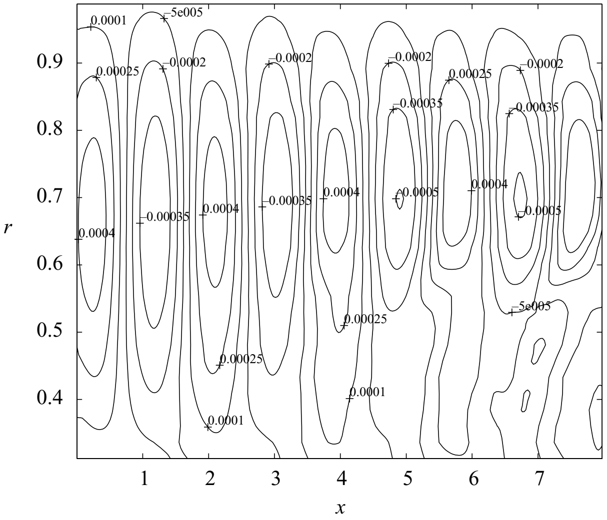

FIGURE 16. Contours of constant-radial-velocity perturbation are shown for a constant-θ or (x, r)-plane of the duct at an instant in time. The dimensionless frequency of the excitation is $\omega r_m/c_0 = 1.0$ and the circumferential wavenumber is $m = 10$. The hub–tip ratio of the duct is 0.3.

the neighbourhood of $r = 0.75$ the level of the contours decreases up to $x = 4$ and then there is less observable change in magnitude. Overall, the amplitude of the wave does not grow as clearly as in the low-azimuthal-wavenumber cases. This suggests that the growth in the velocity fluctuations depends strongly on the azimuthal wavenumber of the incident disturbance.

4.3.4. *Nonlinear effects of wave propagation: amplitude dependence*

In the results discussed above, the amplitudes of the incident waves were chosen to be small so that the propagation of the disturbances was well approximated by linear analysis. In what follows, we impose initial amplitudes of 0.005 and 0.009, five and nine times larger than in § 4.3.3, to see whether nonlinear effects are visible even at these relatively small initial amplitudes. Figures 17–20 show contours of the density and axial velocity for the ‘large’ amplitude waves. As in the small-amplitude case, $a = 0.001$, the disturbances propagate as unstable waves and their amplitude is approximately five times larger at the exit of the domain. This growth occurs near the mean radius of the duct, where the largest gradients in mean density and velocity occur. Near the hub and tip, where the gradients become small, the amplitude of the density fluctuation is an order of magnitude smaller than the amplitude near the mean radius and does not change from that imposed at the inlet.

In linear problems the solutions are amplitude independent. In the general nonlinear problem, clear differences exist between the propagation of the disturbances seen in figures 8–10 and those seen in figures 17–20. Steepening of the wave fronts is visible in both cases with ‘large’ amplitude excitations, as the wave propagates downstream. This is especially visible in the larger-amplitude case, $a = 0.009$, shown in figures 19 and 20, where very steep gradients occur and the concentrated regions of high density and velocity magnitude appear like shock waves as they propagate downstream. As the amplitude is increased, this steepening is noticeable closer to the inlet and is more pronounced. For example, in the small-amplitude case the density contours

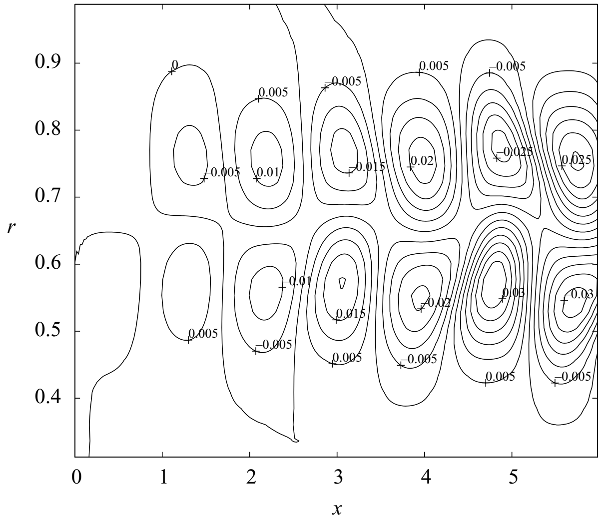

Figure 17. Contours of constant-density perturbation are shown for waves with amplitude $a = 0.005$ for a constant-θ or (x, r)-plane of the duct at an instant in time. The dimensionless frequency of the excitation is $\omega r_m/c_0 = 1.0$ and the circumferential wavenumber is $m = 1$. The hub–tip ratio of the duct is 0.3.

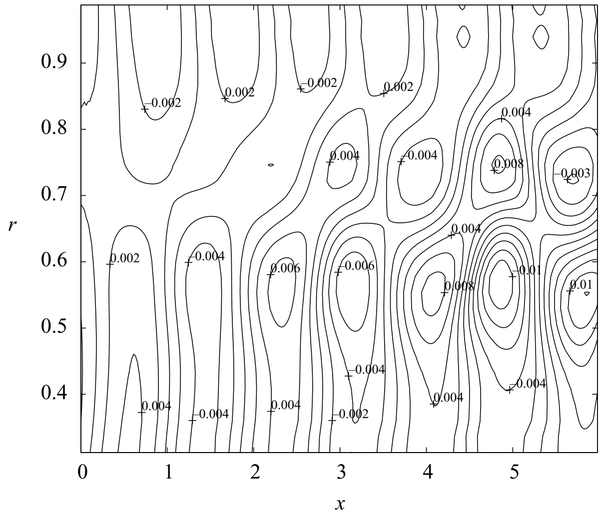

Figure 18. As figure 17 but showing contours of constant-axial-velocity perturbation.

grow in nearly circular shapes near mid-radius. However, in the large-amplitude case the contours are distorted and form a more elliptical shape, whose minor axis is in the x-direction and whose major axis is in the radial direction. To see more clearly the steepening in the axial direction, in figure 21 and 22 we show line plots, at a constant radial location, of the density and axial velocity. In both figures the slope of the wavefront steepens downstream and sharp density and axial-velocity fronts are visible. From characteristic analysis of the one-dimensional Euler equations, it may be

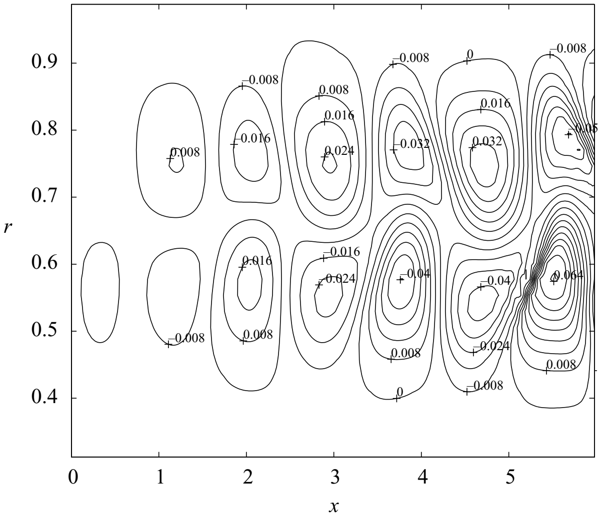

FIGURE 19. Contours of constant-density perturbation are shown for waves with amplitude $a = 0.008$ for a constant-θ or (x, r)-plane of the duct at an instant in time. The dimensionless frequency of the excitation is $\omega r_m / c_0 = 1.0$ and the circumferential wavenumber is $m = 1$. The hub–tip ratio of the duct is 0.3.

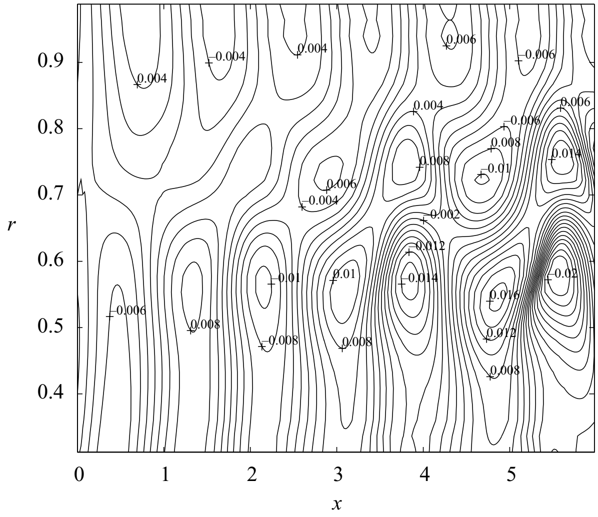

FIGURE 20. As figure 19 but showing contours of constant-axial-velocity perturbation.

shown that ‘nonlinear steepening of the waves eventually leads to wave breaking’ with multivalued solutions (Whitham 1974). Since multivalued solutions are not possible, a shock must be formed at the location of the wavefront. However, as the slope of the wavefront becomes very large, viscous and heat-conduction effects become important and determine the local structure of the shock. Computational Euler methods, like the one presented in this paper, utilize artificial dissipation to capture the steepening wavefronts and prevent overturning (Jameson, Schmidt & Turkel 1981).

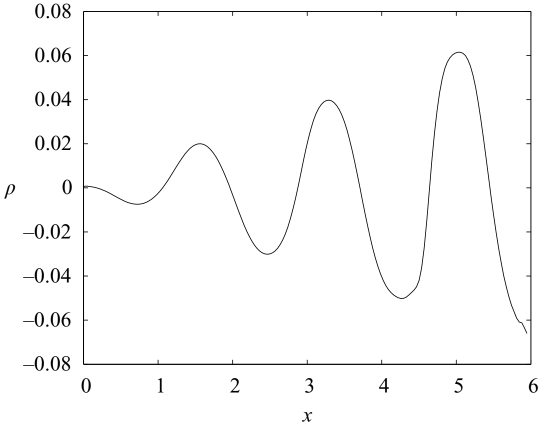

FIGURE 21. A line plot of the density is shown at an instant in time. The dimensionless frequency of the excitation is $\omega r_m/c_0 = 1.0$ and the circumferential wavenumber is $m = 1$. The hub–tip ratio of the duct is 0.3.

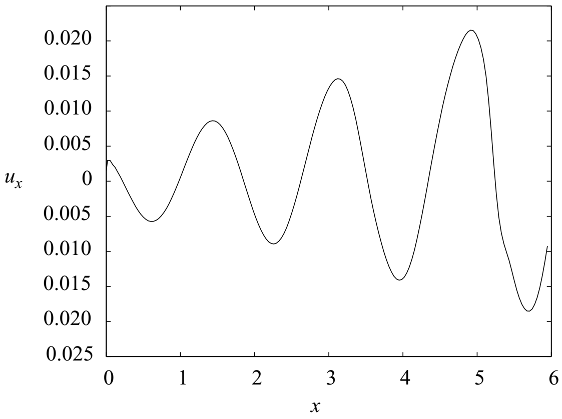

FIGURE 22. A line plot of the axial-velocity perturbation at an instant in time. The dimensionless frequency of the excitation is $\omega r_m/c_0 = 1.0$ and the circumferential wavenumber is $m = 1$. The hub–tip ratio of the duct is 0.3.

5. Conclusions

Vortical disturbances result whenever a fluid passes over bodies or structures and entropy disturbances occur whenever temperature gradients exist in the mean flow or there are heat sources such as flames. Thus, the presence of entropic and vortical disturbances should be ubiquitous in heated internal flows. Understanding the propagation of these convective disturbances resulting from upstream sources is important. Radial temperature gradients couple vortical and entropic disturbances through the radial-velocity perturbation and result in growing density fluctuations even when the mean flow velocity is uniform. Thus, initially vortically dominated disturbances generate significant entropy fluctuations owing to the mean-temperature gradients. The growth in these disturbances eventually produces amplitudes large enough to result in significant nonlinear steepening, which in turn results in large gradients between wavefronts. Pure entropy waves without a velocity perturbation do not exhibit growth and coupling with the velocity field as they propagate downstream. Instead they convect downstream with constant amplitude.

The velocity fluctuations are modified by the mean-velocity profile and the azimuthal wavenumber and are coupled to the entropy waves. They exhibit instabilities when there is an inflection point in the mean-velocity profile, and the largest growth occurs with reduced frequencies and spinning-mode orders close to unity. As these unstable waves grow, significant nonlinear steepening occurs, which results in large gradients between wavefronts. The growth in the velocity is affected by the azimuthal wavenumber and, owing to the coupling between the vortical velocity and density, the growth in the entropy waves is also altered.

Understanding the propagation of these disturbances is an important first step towards studying how efficiently they scatter into acoustic waves in the presence of geometrical changes, which occur in nozzles or cavities, or flames. Moreover, the results suggest that mean flows with radial temperature gradients can destabilize perturbations and lead to large-amplitude disturbances. This is especially noticeable in the low-order circumferential modes, whose variations scale with the mean radius of the duct. Since these low-order modes are often the most problematic in combustion instabilities, we suggest that understanding the effects of the radial profiles in the mean flow may be important in these applications.

This work was supported by the Ramon y Cajal fellowship while the author was at the University of Seville. The author would like to thank Professor Antonio Barerro for the stimulating research environment during his stay at the University of Seville.

REFERENCES

Atassi, H. M., Ali, A. A., Atassi, O. V. & Vinogradov, I. V. 2004 Scattering of incident disturbances by an annular cascade in a swirling flow. *J. Fluid Mech.* **499**, 111–138.

Atassi, O. V. 2003 Computing the sound power in non-uniform flow. *J. Sound Vib.* **266**, 75–92.

Atassi, O. V. 2004 Nonreflecting boundary conditions for the time-dependent wave equation. *J. Comput. Phys.* **197**, 737–758.

Atassi, O. V. & Ali, A. 2002 Inflow/outflow conditions for internal time-harmonic Euler equations. *J. Comput. Acoust.* **10**, 155–182.

Atassi, O. V. & Galan, J. M. 2005 Nonreflecting boundary conditions for the euler equations. *AIAA Paper* 2005–1585.

Cooper, A. J. & Peake, N. 2001 Propagation of unsteady disturbances in a slowly varying duct with mean swirling flow. *J. Fluid Mech.* **445**, 207–234.

Cooper, A. J. & Peake, N. 2005 Upstream-radiated rotor–stator interaction noise in mean swirling flow. *J. Fluid Mech.* **523**, 219–250.

Drazin, P. & Reid, D. 1984 *Hydrodynamic Stability*. John Wiley & Sons.

Ellingsen, T. & Palm, E. 1975 Stability of linear flow. *Phys. Fluids* **18**, 487–488.

Golubev, V. V. & Atassi, H. M. 1998 Acoustic-vorticity waves in swirling flows. *J. Sound Vib.* **209**, 203–222.

Hanifi, A. & Henningson, D. 1998 The compressible inviscid algebraic instability for streamwise independent disturbances. *Phys. Fluids* **10**, 1784–1786.

Jameson, A., Schmidt, W. & Turkel, E. 1981 Numerical solution of the euler equations by finite volume methods using runge-kutta time stepping schemes. *AIAA Paper* 81-1259.

Kerrebrock, J. L. 1977 Small disturbances in turbomachine annuli with swirl. *AIAA J.* **15**, 794–803.

Kovàsnznay, L. S. G. 1953 Turbulence in supersonic flow. *J. Aero. Sci.* **20**.

Landahl, M. 1980 A note on an algebraic instability of inviscid parallel shear flows. *J. Fluid Mech.* **98**, 243–251.

Lin, H. & Szeri, A. J. 2001 Shock formation in the presence of entropy gradients. *J. Fluid Mech.* **431**, 161–188.

MARBLE, F. & CANDEL, S. 1977 Acoustic disturbance from gas non-uniformities convected through a nozzle. *J. Sound Vib.* **55**, 225–243.

RIENSTRA, S. W. 1999 Sound transmission in slowly varying circular and annular lined ducts with flow. *J. Fluid Mech.* **380**, 279–296.

RIENSTRA, S. W. & EVERSMAN, W. 2003 Sound propagation in slowly varying lined flow ducts with arbitrary cross section. *J. Fluid Mech.* **495**, 157–173.

SOUKHOMLINOV, V., KOLOSOV, V., SHEVEREV, V. & OTUGEN, M. 2002 Formation and propagation of a shock wave in a gas with temperature gradients. *J. Fluid Mech.* **473**, 245–264.

STOW, S. R., DOWLING, A. P. & HYNES, T. P. 2002 Reflection of circumferential modes in a choked nozzle. *J. Fluid Mech.* **467**, 215–239.

TYAGI, M. & SUJITH, R. 2003 Nonlinear distortion of travelling waves in variable-area ducts with entropy gradients. *J. Fluid Mech.* **492**, 1–22.

VILENSKI, G. & RIENSTRA, S. W. 2005 Acoustic modes in a ducted shear flow. *AIAA Paper* 2005–3024.

WHITHAM, G. B. 1974 *Linear and Nonlinear Waves*. John Wiley & Sons.